Acta Mech. Sin. (2011) 27(6):845–865
DOI 10.1007/s10409-011-0522-0

REVIEW

Surrogate-based modeling and dimension reduction techniques for multi-scale mechanics problems

Wei Shyy · Young-Chang Cho · Wenbo Du · Amit Gupta · Chien-Chou Tseng · Ann Marie Sastry

Received: 7 September 2011 / Revised: 9 September 2011 / Accepted: 15 September 2011

Abstract Successful modeling and/or design of engineering systems often requires one to address the impact of multiple "design variables" on the prescribed outcome. There are often multiple, competing objectives based on which we assess the outcome of optimization. Since accurate, high fidelity models are typically time consuming and computationally expensive, comprehensive evaluations can be conducted only if an efficient framework is available. Furthermore, informed decisions of the model/hardware's overall performance rely on an adequate understanding of the global, not local, sensitivity of the individual design variables on the objectives. The surrogate-based approach, which involves approximating the objectives as continuous functions of design variables from limited data, offers a rational framework to reduce the number of important input variables, i.e., the dimension of a design or modeling space. In this paper, we review the fundamental issues that arise in surrogate-based analysis and optimization, highlighting concepts, methods, techniques, as well as modeling implications for mechanics problems. To aid the discussions of the issues involved, we summarize recent efforts in investigating cryogenic cavitating flows, active flow control based on dielectric barrier discharge concepts, and lithium (Li)-ion batteries. It is also stressed that many multi-scale mechanics problems can naturally benefit from the surrogate approach for "scale bridging."

W. Shyy
Hong Kong University of Science and Technology,
Clear Water Bay, Hong Kong, China
e-mail: weishyy@ust.hk

Y.-C. Cho · W. Du · A. Gupta · A.M. Sastry
University of Michigan, Ann Arbor, MI, USA

C.-C. Tseng
National Taiwan Sun Yat-Sen University,
Kaohsiung, Taiwan, China

Keywords Multi-scale mechanics · Cryogenic cavitating flow · Surrogate-based modeling · Active flow control · Engineering system

Nomenclature

b	Vector of polynomial coefficients
C	Cycling rate, where 1C is the rate required to charge/discharge the cell in one hour
D	Characteristic length scale (m)
D_s	Solid diffusion coefficient (m^2/s)
E	Expectation value
f_v	Vapor mass fraction/Frequency of applied voltage (kHz)
F_x	x-directional Lorentzian force (mN/m)
$F_{x,S}$	Domain averaged x-directional Lorentzian force (mN/m)
$F_{x,ST}$	Time and domain averaged x-directional Lorentzian force (mN/m)
h	Enthalpy (kJ/kg)
L	Latent heat (kJ/kg)
m^+	Source term in cavitation model (1/s)
m^-	Sink term in cavitation model (1/s)
n_p	Particle number density of species p (1/m^3)
N_s	Number of sampled design points
N_{RBF}	Number of neural basis functions
N_v	Number of design variables
P	Pressure (N/cm^2); power input due to the charge current through the upper electrode (W)
P_v	Saturation vapor pressure (N/cm^2)
P_{diff}	L_2 norm between experiment and predicted pressure (N/cm^2)
P_T	Time averaged power input due to the charge current through the upper electrode (W)
Pr	Prandtl number
r_f	Positive-to-negative polarity time ratio of applied voltage waveform
R^2_{adj}	Adjusted coefficient of determination
$R_{s,p}$	Solid particle radius in positive electrode (μm)

$\boldsymbol{s}$	Vector of neuron position
S	Area of computational domain for gas (m^2)
S_M	Main sensitivity index
S_T	Total sensitivity index
t_∞	Reference time scale, $t_\infty = D/U_\infty$ (s)
T	Temperature (K) Period of applied voltage (s)
T_{diff}	L_2 norm between experiment and predicted temperature (K)
u	Velocity (m/s)
u_p	Particle bulk velocity of species p, $(u_{x,p}, u_{y,p}, u_{z,p})$ (m/s)
U_∞	Reference velocity (m/s)
V	Variance
V_{app}	Applied voltage to the upper electrode (kV)
$\boldsymbol{x}$	Vector of design variables; Space variable (m)
y	Objective function
$\hat{y}$	Surrogate approximation of objective function
$\overline{y}$	Mean value of objective function
z	Systematic departure
α_l	Liquid volume fraction
β	Spread coefficient of radial basis neural network
ε_d	Dielectric constant of insulator
μ	Dynamic viscosity (kg/ms)
ρ	Density (kg/m^3)
σ	Electronic conductivity (S/m)
σ_∞	Cavitation number based on the free stream temperature
σ_a	RMS error of polynomial response surface at sampled points
τ	Dimensionless time

1 Introduction

The notion of design variables influencing system performance can be found in numerous thermo-fluid and energy systems. In the computational modeling context, the design variables can be adjustable parameters associated with a given mathematical model under different operating conditions and scaling parameters. In the hardware design context, they are often geometry, materials, and operating variables. In both situations, there are often multiple, competing objectives based on which we assess the outcome of optimization. Since accurate, high fidelity models are typically time consuming and computationally expensive, comprehensive evaluations can be conducted only if an efficient framework is available. This is especially true in the case of multi-scale problems involving physical phenomena occurring at multiple length or time scales, which may need to be computed separately. Furthermore, informed decisions concerning a model or hardware system's overall performance rely on an adequate understanding of the global, not local, sensitivity of the individual design variables on the objectives.

In reality, most engineering system and modeling designs are conducted as open loop, feed-forward processes. For example, for turbine design in aerospace and mechanical engineering, one design iteration for a given set of engine balance conditions may currently take up to several weeks, with just the blade geometry design sub-iteration phases taking several days each. The quest for an acceptable blade surface velocity distribution is accomplished with many ad hoc rules in what is essentially a manual trial-and-error process. A systematic approach capable of identifying design optimality and comparing possible trade-offs can significantly improve productivity and shorten the design cycle.

Objective and efficient evaluation of advanced designs can be facilitated by development and implementation of systematic optimization and sensitivity evaluation methods. To date, the majority of the effort in design optimization has relied on gradient-based search algorithms. These methods work iteratively through a sequence of local sub-problems, which approximate objective and constraint functions for a sub-region of the design space, e.g., by linearization using computed sensitivities. Major challenges for these optimization approaches are the robust and speedy computation of sensitivity coefficients [1].

Yet despite recent research advances, formal design optimization has yet to see practical use in real design scenarios. The reasons are several-fold:

(1) The objective functions are likely to be multi-modal or discontinuous over the broad design space [2], rendering gradient search methods insufficient by themselves. Additionally, the usual practice to combine multiple goals into a single quantitative objective function is too restrictive. Qualitative goals are often required to correctly characterize a problem (e.g., maximizing a turbine blade's aerodynamic efficiency with a smooth, monotonic surface velocity distribution, while spreading heat load as uniformly as possible). These goals may have arisen from diverse disciplines and are usually treated sequentially by different groups.

(2) It is inadequate to think of the final product of a design process as a mere geometry. A "design" really encompasses a whole set of operating, manufacturing, and project level decisions.

(3) As the interaction between numerical simulation and physical test data becomes stronger, the future engineering knowledge base is likely to consist of various heterogeneous data sources including experimental data, past product experiences, semi-empirical modeling, and high fidelity simulations. Some data are anecdotal; others cover only small "patches" of the physical domain but are still useful for "reality checks". A unified framework needs to be constructed for representation, capturing and mining of all these data types so the response functions can be continuously improved.

The surrogate-based approach is an excellent technique for analysis and probing of such issues. It also offers a rational framework to reduce the number of important input variables, i.e., the dimension of a design or modeling space. The surrogates can be constructed using data drawn from pre-computed high-fidelity simulations and physical measurements, and provide fast evaluations of the various modeling and design scenarios, thereby making sensitivity and optimization studies feasible. As discussed by Shyy et

al. [3], they have several advantages when compared to local gradient-based methods:

(1) They do not require calculation of the local sensitivity of each design variable;

(2) They can utilize the information collected from various sources and by different tools;

(3) They offer multi-criterion optimization;

(4) They can handle the existence of multiple design points and trade-offs;

(5) They easily perform tasks in parallel;

(6) They can often effectively filter the noise intrinsic to numerical and experimental data;

(7) They provide an approximation for functions that can be easily used to bridge disparate length or time scales in multi-scale problems.

However, there are uncertainties in predictions using this approach, such as empiricism in computational models and surrogate model errors. We have developed methods to estimate and to reduce such uncertainties using multiple criteria because a single criterion may underestimate the error. We have advanced the techniques of using an ensemble of surrogates to reduce uncertainties in selecting the best surrogate and sampling strategy. We have also developed an averaging technique for multiple surrogates that protects against poor surrogates and performed at par with the best surrogate for many problems.

In this paper, we discuss the fundamental issues that arise in surrogate-based analysis and optimization, highlighting concepts, methods, and techniques, as well as practical implications. Our focus here is on multi-scale mechanics problems, instead of practical device design and optimization. Furthermore, to aid the discussions of the issues involved, we will summarize recent efforts in investigating cryogenic cavitating flows, active flow control based on dielectric barrier discharge concepts, and lithium (Li)-ion batteries. In cavitating flows of cryogenic fluids, such as liquid nitrogen and hydrogen, thermal effects are very important. Surrogate-based analysis has been used to investigate the importance of two adjustable parameters, which regulate the strength of the evaporation and condensation rate in the cavitation model, and the sensitivity of the thermal-sensible fluid properties, including latent heat and vapor phase density. The surrogate-based strategy has also been used to establish appropriate values for these empirical constants. For the dielectric barrier discharge (DBD) actuator, the impact of the applied voltage frequency, the insulator dielectric constant and the polarity time ratio of the voltage waveform on the net force generation and required power are examined. Multiple surrogate models consistently identify two branches of the Pareto front where a positive x-directional net force requires relatively low power, while a negative net force requires high power. Moreover, global sensitivity analysis indicates that the voltage frequency and polarity time ratio are important in only some portions of the design space, while the dielectric constant is always important. A Li-ion battery cell has also been analyzed using a surrogate modeling framework to map the effect of cycling rate, cathode particle size, and diffusion coefficient and electrical conductivity of the solid cathode material on the energy density. Through global sensitivity analysis the relative impact of the various parameters can be quantified under different scenarios. The design space is split into distinct regions based on characteristic discharge and diffusion time scales for separate, more refined analysis. A Pareto front is constructed to quantify the tradeoff between maximum achievable energy and power levels. It should also be noted that the surrogate approach offers a natural and effective framework for "scale bridging", which is at the heart of the multi-scale issues arising from many mechanics problems.

The rest of the paper is structured as follows. We first present an overview of the surrogate methodology to highlight the key steps involved. Surrogate tools applied to cryogenic cavitation, flow control using DBD actuators, and Li-ion battery cells are discussed next. We conclude the paper with a summary of key aspects of surrogate analysis that are common to all case studies presented and their relevance to other problems of multi-objective optimization.

2 Surrogate modeling methodology

The key steps in the surrogate modeling process are shown in Fig. 1. The process begins with constructing a set of experimental or numerical experiments, the output data from which are used to train surrogates. Separate experiments may also be conducted to obtain independent test points that are used to compare the relative accuracy of the surrogates and assess their predictive capability. Based on this error assessment, the surrogates may be refined by including data from additional experiments, and used for further analysis.

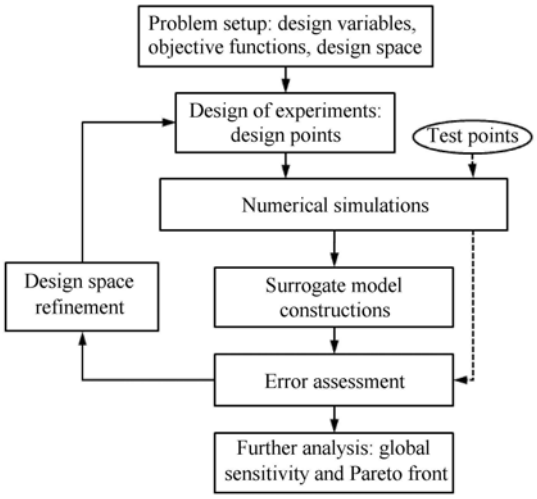

Fig. 1 Flowchart for the surrogate-based modeling framework

2.1 Design of experiments

The design of experiments consists of the design points at which training data for the surrogate models are obtained. In most problems the nature of the objective function is not known beforehand, so it may be simplest to use random sampling of the design space to avoid biased sampling. However, the number of experiments or simulations that can be conducted is often limited, so a more efficient approach is desired. One improvement over pure random sampling is Latin Hypercube sampling (LHS), which provides a random sampling but ensures a stratified sample within the full range of each dimension of the sample space [4].

Although LHS can give a representative sample within design ranges, due to its random nature it does not ensure sampling at the extrema of the parameter space, which may be of critical interest. One method considered in this study for sampling design space boundaries is the two-level face-centered composite design (FCCD), which includes the face-center points and vertices of the design hypercube [5].

2.2 Surrogate models

In general, different types of surrogate models should be attempted and compared if possible, since the best method is problem-dependent (and, as will be seen, region-dependent within a single design space) and can not be predicted beforehand. A brief description of the commonly used models is as follows; further details can be found in Refs. [6,7].

2.2.1 Polynomial response surface (PRS)

In a polynomial response surface model, the objective function is approximated as a linear combination of polynomial basis functions

$$\hat{y}(\boldsymbol{x}) = \sum_i b_i f_i(\boldsymbol{x}). \tag{1}$$

The number of i terms and the maximum degree of $f_i(\boldsymbol{x})$ are determined by the order of the PRS model. There often exists an "optimum" polynomial order; higher-order polynomial response surfaces can potentially achieve greater accuracy by allowing more degrees of freedom, but can also suffer from excessive curvature that can hinder accuracy and show inconsistent trends in the objective function from actual data. The coefficient vector $\boldsymbol{b}$ is selected using a least squares method such that the prediction error at the training data points is minimized.

The adjusted coefficient of determination quantifies the prediction capability of the polynomial response surface approximation. This parameter is defined to account for the number of sample points

$$R^2_{\text{adj}} = 1 - \frac{\sigma^2_{\text{a}}(N_{\text{s}} - 1)}{\sum_{i=1}^{N_{\text{s}}} (y_i - \bar{y})^2}. \tag{2}$$

A good polynomial fit should have a small RMS error, and thus an R^2_{adj} value close to 1.

2.2.2 Kriging (KRG)

In a kriging model, the objective function is approximated as a sum of a polynomial regression model and a systematic departure $Z(\boldsymbol{x})$ (or a set of basis functions [8])

$$\hat{y}(\boldsymbol{x}) = \sum_i b_i f_i(\boldsymbol{x}) + Z(\boldsymbol{x}). \tag{3}$$

The systematic departure components are assumed to be correlated as a function of distance between the locations under consideration, and the maximum likelihood estimation is used to determine the parameter estimates [9]. In this study a variety of correlation functions are considered: Gaussian, linear, exponential, cubic, (cubic) spline, and spherical. A detailed formulation of these correlation functions has been summarized by Lophaven et al. [10].

2.2.3 Radial-basis neural network (RBNN)

A radial-basis neural network model approximates the objective function as a linear combination of radial basis functions [11], also known as neurons

$$\hat{y}(\boldsymbol{x}) = \sum_{i=1}^{N_{\text{RBF}}} w_i a_i(\boldsymbol{x}). \tag{4}$$

The Gaussian function has been used as the radial basis function in this study

$$a_i(\boldsymbol{x}) = \mathrm{e}^{-(\|\boldsymbol{s}_i - \boldsymbol{x}\|\beta)^2}, \tag{5}$$

where the quantity $\|\boldsymbol{s}_i - \boldsymbol{x}\|$ is the distance to the i-th radial basis function. The number of neurons and associated weights are determined by satisfying the user defined error "goal" on the mean squared error in approximation.

2.2.4 PRESS weighted surrogates (PWS)

Weighted average surrogate models combine information from multiple individual surrogates via a weighting scheme to reduced uncertainties in selecting the best model based on limited validation criteria. Various weighting strategies are possible; we adopt a method based on the PRESS values of the individual surrogates. Further details of weighting strategies for multiple surrogates can be found in Ref. [12].

2.3 Cross-validation

In order to select appropriate surrogate models for analysis, methods for evaluating and comparing the accuracy of the models are required. Procedures for comparing error measures for kriging and PRS models have been developed by Goel et al. [13]. One common strategy is to obtain simulation data at test points, which are sampled independently from design points as a validation data set. The prediction

error could then be computed at each test point for each surrogate model. While this method is easy to use and is useful for performing cross-validation, it is also limited by the number of test points, which usually are computationally expensive to obtain. The use of other cross-validation techniques in conjunction with test-point prediction error has also been adopted.

To estimate the accuracy of a surrogate model independent of test points, a parameter S_{press} called the prediction error sum of squares can also be computed. PRESS is computed directly from the training data by summing the "leave-one-out" prediction errors at all data points. The "leave-one-out" prediction error is defined as the prediction error at a particular point using the surrogate model constructed from all other data points. In a more general formulation allowing an arbitrary number of data points to be left out at a time, this parameter is known as the generalized mean square error (GMSE). In this study, we use the PRESS (RMS) value as the basis of evaluation and comparison

$$S_{\text{press}} = \sqrt{\frac{1}{N_{\text{s}}} \sum_{i=1}^{N_{\text{s}}} \left(y_i - \hat{y}_i^{(-i)}\right)^2}, \tag{6}$$

where $\hat{y}_i^{(-i)}$ represents the prediction at $\boldsymbol{x}^{(i)}$ using the surrogate constructed using all sample points except $(\boldsymbol{x}^{(i)}, y_i)$. When the number of design points are sufficiently large, it is also possible to leave out a group of partitioned data [14] or every possible combination of multiple design points (leave-k-out approaches [15]) for cross-validation.

2.4 Global sensitivity analysis

Global sensitivity analysis can be useful for comparing the relative magnitude of effect of the design variables on the objective function, especially if the number of design variables is large. Variables that have little effect on the objective function can be identified and removed from consideration, allowing the design space to be reduced. A method similar to that used by Sobol [16] has been employed in this work.

An objective function f (obtained from the surrogate model) can be decomposed as a sum of functions of individual variables and combinations of variables, known as additive functions

$$f(\boldsymbol{x}) = f_0 + \sum_i f_i(x_i) + \sum_{i<j} f_{ij}(x_i, x_j) + \cdots + f_{1\cdots N_{\text{v}}}(x_1, x_2, \cdots, x_{N_{\text{v}}}), \tag{7}$$

where the total variance $V(f)$ is defined as the expected value of the square of the summation of all non-zero order additive functions. The total variance can also be expressed as a sum of partial variances of the individual variables and combinations of variables

$$V(f) = \sum_{i=1}^{N_{\text{v}}} V_i + \sum_{i<j} V_{ij} + \cdots + V_{1\cdots N_{\text{v}}}. \tag{8}$$

The partial variances are in turn defined in terms of the expected value of the additive functions

$$\begin{aligned} V_i &= V(E[f|x_i]), \\ V_{ij} &= V(E[f|x_i, x_j]) - V_i - V_j, \\ &\cdots . \end{aligned} \tag{9}$$

The expected values of the additive functions and their variances can be expressed as integrals of the additive functions which are approximated using a five point Gauss quadrature scheme in this study

$$E[f|x_i]_i = \int_0^1 f_i(x_i)\mathrm{d}x_i, \tag{10a}$$

$$V(E[f|x_i]_i) = \int_0^1 f_i^2(x_i)\mathrm{d}x_i. \tag{10b}$$

The main sensitivity indices can then be computed from the partial variances

$$S_{\text{M}i} = \frac{V_i}{V(f)}, \tag{11}$$

whereas the total sensitivity index for the i-th variable is defined as the sum of all variance terms involving i, divided by the total variance. This can be expressed as a sum of the main sensitivity index and all higher-order terms involving i

$$S_{\text{T}i} = S_{\text{M}i} + \frac{\sum_{j,j\neq i} V_{ij} + \cdots}{V(f)}. \tag{12}$$

The relative importance of the design variables can be observed by comparing either their partial variances (main sensitivity indices) or their total variances (total sensitivity indices). The difference between the main and total sensitivity indices for each variable also gives an indication of the degree of interaction between variables.

2.5 Pareto front

A single continuous objective function obtained through surrogate-based modeling may be further optimized by simply searching the design space for the minimum or maximum value of the objective. However, if multiple competing objectives are present, there may be no single optimal design, but many designs in which one objective is improved at the cost of another [17]. Pareto-optimal solutions (also known as Pareto-efficient solutions) comprise the set of designs that are not dominated by any other design. A design is said to be dominated by another if it is no better in any objectives, and worse in at least one objective. The set of Pareto-optimal solutions can be used to construct a Pareto front, which represents all optimal combinations of the objectives if their relative importance is not known. In the surrogate modeling framework, a surrogate model can also be utilized to construct the Pareto front in addition to the existing training data. Inspection of the Pareto front may then

reveal the existence of favorable tradeoffs between the competing objectives, and assist significantly in the optimization process.

3 Case studies to demonstrate surrogate modeling techniques

Having introduced the methodology and basic concepts, we now present different scenarios where the surrogate-based modeling and optimization has been used to study the interplay of independent variables and their influence on the desired objective(s) for cases that include cavitation in cryogenic fluids, dielectric barrier discharge actuator and modeling of Li-ion cells. A brief overview of the motivation and methods used in each study has been outlined, followed by a discussion of the key findings and summary of the contributions provided by the surrogate-based framework.

3.1 Cavitation in cryogenic fluids

Cryogenic liquids, including liquid oxygen, nitrogen, and hydrogen, are used as liquid rocket propellants due to their high power density and clean by-products. A key design issue surrounding rocket fuel and oxidizer pumps is the minimum pressure that the design can tolerate for a given inlet temperature and rotational speed. To keep inlet pressure low (reducing tank weight) and pump rotational speeds high (reducing engine weight), cavitation, which occurs when the local pressure in a fluid is lower than the vapor pressure [18–23], is prone to appear in the inducer section. When this occurs, the forming vapor phase will replace the liquid inside the cavity; in order to maintain the vapor phase, the surrounding liquid will adjust its thermodynamic state and experience evaporative cooling, causing a temperature drop in the surrounding area. Although various cavitation models have been categorized and documented, for example in Refs. [24–29], there is, to date, no established method capable of predicting the actual loads due to cavitation on the inducer blades. The unsteadiness of the cavitating pump can be coupled with the feed or discharge system, causing large component oscillations. Furthermore, thermal effects are much stronger in cryogenic cavitating liquids than in conventional liquids such as water due to the thermal-sensibility of properties such as vapor pressure and reduced liquid-vapor density ratios under such conditions [26].

Due to the complexity of the flow phenomena, validated computational tools capable of predicting cavitating flow behavior are necessary for rocket fuel-oxidizer pump design. In this study we seek to use surrogate modeling tools to assess and improve the predictive capabilities of a cavitation model with respect to model parameters by comparing the output to experimental data.

3.1.1 Physical model

The Navier–Stokes equations are well established for multiphase fluid dynamics. The set of governing equations for the cavitation computation under the homogeneous-fluid modeling consists of the conservative form of the Favre-averaged Navier–Stokes equations, the enthalpy-based energy equation for cryogenic cavitation, the k–ε two-equation turbulence closure, and a suitable cavitation model. The details are well-documented in Refs. [24–28]. Generally, a cavitation model is a transport equation for the liquid volume fraction , which can be written in the following form

$$\frac{\partial(\alpha_\mathrm{l})}{\partial t} + \frac{\partial(\alpha_\mathrm{l} u_j)}{\partial x_j} = m^+ + m^-. \tag{13}$$

Fluid mixture properties, such as mixture density, can be evaluated based on the liquid volume fraction, vapor phase density ρ_v, and liquid phase density ρ_l

$$\varphi_\mathrm{m} = \varphi_\mathrm{l}\alpha_\mathrm{l} + \varphi_\mathrm{v}(1-\alpha_\mathrm{l}), \tag{14}$$

where the source (m^+) and sink (m^-) terms correspond to the condensation and evaporation rates, respectively. Multiple studies documented in Refs. [24–29] have modeled the liquid volume fraction α_l(or vapor volume fraction) via the sink and source terms, which regulate the mass transfer between vapor and liquid phases with empirical constants. Liquid-vapor evaporation and condensation rates for this transport-based cavitation model can be written in the following form

$$\begin{aligned} m^- &= \frac{C_\mathrm{dest}\alpha_\mathrm{l}}{t_\infty}\frac{\rho_\mathrm{l}}{\rho_\mathrm{v}}\frac{\min(0, P-P_\mathrm{v})}{(0.5\rho_\mathrm{l}U_\infty^2)}, \\ m^+ &= \frac{C_\mathrm{prod}(1-\alpha_\mathrm{l})}{t_\infty}\frac{\max(0, P-P_\mathrm{v})}{(0.5\rho_\mathrm{l}U_\infty^2)}, \end{aligned} \tag{15}$$

where P is the local pressure and P_v is the vapor pressure. U_∞ is the reference velocity scale, and t_∞ is the reference time scale, defined as the characteristic length scale D divided by the reference velocity scale. The conditional statements in the source and sink terms indicate that evaporation occurs when the pressure is less than the vapor pressure, and that condensation occurs when the pressure is greater than the vapor pressure, under the assumption of thermal equilibrium. Based on current flow conditions, the cavitation is attached, and hence the steady-state calculation is used. Note that in addition to the fluid properties and flow parameters, Eq. (15) also relies on two empirical constants, C_dest and C_prod. Furthermore, C_dest and C_prod are material dependent constants [24–26].

In the case of cryogenic cavitation, the thermal effects can not be neglected and an additional equation is required

$$\frac{\partial}{\partial x_j}[\rho_\mathrm{m} u_j(h + f_\mathrm{v}L)] = \frac{\partial}{\partial x_j}\left[\left(\frac{\mu_\mathrm{L}}{Pr_\mathrm{L}} + \frac{\mu_\mathrm{T}}{Pr_\mathrm{T}}\right)\frac{\partial h}{\partial x_j}\right]. \tag{16}$$

Note in Eq. (16) that the subscripts “L” and “T” indicate laminar and turbulent flow, respectively. The temperature T can be computed based on the enthalpy h [23], and the vapor mass fraction is expressed as

$$f_v = \frac{\rho_v(1-\alpha_l)}{\rho_m}. \quad (17)$$

In summary, this homogeneous fluid cavitation model consists of the conservative form of the Favre-averaged Navier–Stokes equations, the enthalpy-based energy equation for cryogenic cavitation, the k–ε two-equation turbulence closure based on a filter approach [24–28], and a transport equation for the liquid volume fraction. More details of cavitation modeling can be found in Refs. [24–28].

In this study, we use surrogate modeling techniques to assess the influence of parameters regulating the condensation and evaporation rates and uncertainties in material properties on the performance of the transport-based cryogenic model.

3.1.2 Surrogate modeling process

(a) Design of experiments and cross-validation

In this study we consider cryogenic cavitation with thermal effects in a 2D domain. A schematic of this problem setup is illustrated in Fig. 2. Two cases corresponding to experimental data reported in Ref. [30] are investigated with the conditions listed in Table 1. In both cases the working fluid is liquid nitrogen, and the computational domain consists of 2×10^4 structured grid elements.

Table 1 Cryogenic cavitation cases conditions

Case	σ_∞	Re	T_∞/K
290C	1.70	9.1×10^6	83.06
296B	1.61	11.0×10^6	88.54

Since we wish to assess the overall predictive performance of the cavitation model, the objective functions of interest are the RMS values of the differences between computed and experimental [30] temperature (T_{diff}) and pressure (P_{diff}) values, evaluated at five different locations along the hydrofoil surface shown in Fig. 2.

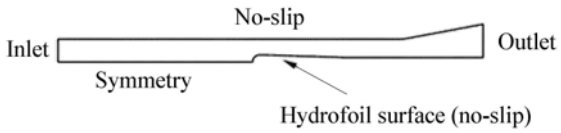

Fig. 2 Schematic of the geometry and boundary conditions

Table 2 lists the design variables considered and their ranges, as well as the objective functions. The ranges of the two empirical constants C_{dest} and C_{prod}, which directly control the evaporation and condensation rates in the cavitation model, are selected in accordance with those found in Ref. [30]. The effects of perturbations in the fluid properties are also examined by varying the vapor density, which dominates the evaporating cooling term and also appears directly in the cavitation sink term, and latent heat, which determines the energy absorbed or released during the phase change, relative to the NIST database values [23].

Table 2 Objective functions and design variables with corresponding ranges

Symbol	Design variable	Range
C_{dest}	Evaporation rate	0.578–0.680
C_{prod}	Condensation rate	46.2–54.4
P_V	Vapor density*	−10%–10%
L	Latent heat*	−10%–10%
Symbol	**Objective function**	
P_{diff}	Pressure difference between CFD and exp. data	
T_{diff}	Temperature difference between CFD and exp. data	

*: Vapor density and latent heat are relative to database values.

Figure 3 shows the sensitivity of T_{diff} and P_{diff} with respect to the empirical constants for Case 290C without perturbations in material properties. Case 296B also shows similar results. Clearly, the temperature and pressure distribution shows some dependence on the empirical constant values, so no immediate reduction in problem dimensionality is available. An example of a cavity outlook ($C_{\text{dest}} = 0.639$, $C_{\text{prod}} = 54.4$) is also shown in Fig. 3c.

Table 3 Cross-validation measures for surrogates (70 training points)

	P^*_{diff}		T^*_{diff}	
Surrogate	290C	296B	290C	296B
S_{press} PRS/%	6.38	11.90	9.11	10.02
S_{press} KRG/%	2.97	2.93	2.48	6.62
S_{press} RBNN/%	13.91	11.67	13.31	19.03
S_{press} PWS/%	3.97	5.44	5.50	9.20

A design experiments consisting of 70 training data points is selected using a combined FCCD strategy (25 points) and LHS (45 points) by maximizing minimum distances between points. PRS, KRG, RBNN, and PWS models of both objectives in normalized variable space are constructed, and objective function values are also normalized. Second order polynomials for PRS and spread coefficients in the range between 0.4 and 0.7 are considered.

Cross-validation measures are summarized in Table 3. Based on the PRESS criterion, the KRG model is found to have the best overall performance while the RBNN has the worst. Five additional independent test points are also considered for cross-validation; the KRG model also shows the best agreement for both Case 290C and 296B in Ref. [30]. Based on these cross-validation results, the KRG model is selected for global sensitivity analysis.

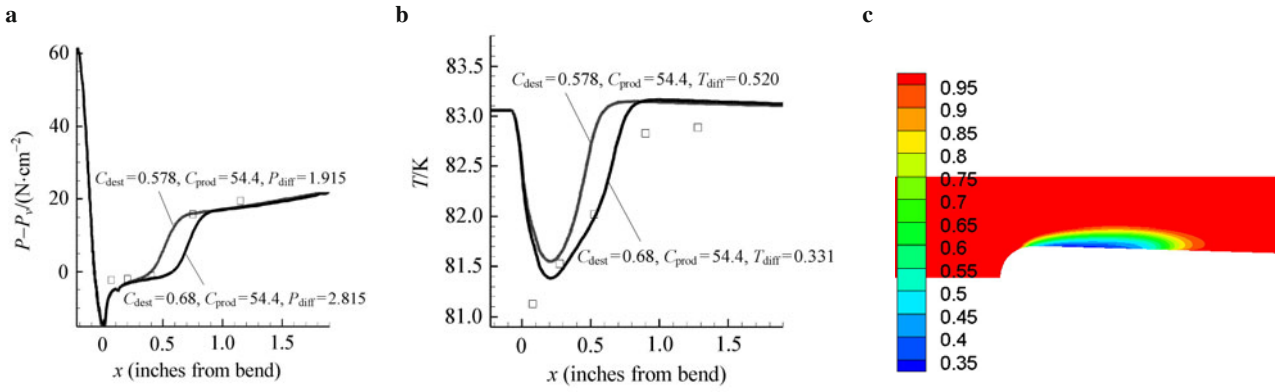

Fig. 3 Cryogenic cavitation cases Case 290C ($\sigma_\infty = 1.7$, $Re = 9.1 \times 10^6$, $T_\infty = 83.06$ K). **a** Pressure; **b** Temperature; **c** Liquid volume fraction

(b) Global sensitivity analysis

Figures 4 and 5 show the overall impact of each design variable on both objectives for Case 290C and 296B, respectively. The overall sensitivity results are similar for the pressure prediction in the two cases, where the effects of the evaporative and vapor density terms are very important while the contributions from the condensation and latent heat terms are much less significant. However, the effect of latent heat on the temperature distribution is much more significant in Case 296B than in Case 290C. Since Case 296B has a greater inlet temperature, this suggests that the sensitivity of the thermal field to thermodynamic properties increases with temperature. In both cases, the condensation term has negligible influence on both objectives, allowing a reduction in problem dimensionality.

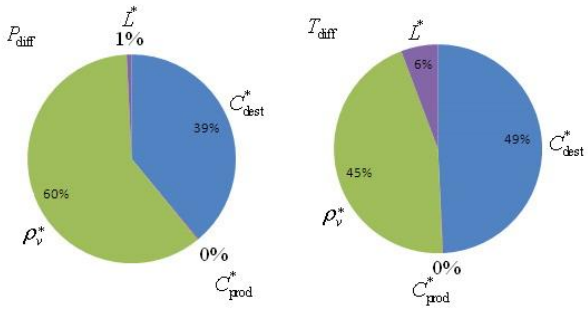

Fig. 4 Global sensitivity indices for Case 290C

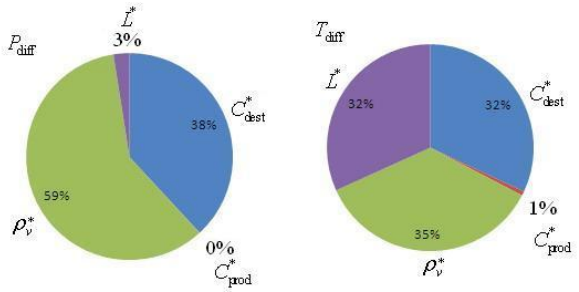

Fig. 5 Global sensitivity indices for Case 296B

(c) Dimensionality reduction

In the next step of the surrogate process, we can optimize the evaporative term C_{dest} within its design range to minimize the pressure and temperature discrepancies between computed results and experimental data. Since the condensation term does not influence the performance of the present cryogenic cavitation model, it is appropriate to fix its value ($C_{prod} = 54.4$). Additionally, since material properties are not variables that can be tuned for optimization and are studied only to compare the relative sensitivity of the pressure and temperature distribution to uncertainties in these properties, we fix the temperature-dependent material properties ρ_v and L to values obtained from the NIST database [23].

The two objectives are plotted against the evaporative term for both cases in Fig. 6. Note that while in Case 296B the two objectives show a similar trend to each other, they show very different trends in Case 290C. Due to these opposing trends, the optimal value for C_{dest} depends on which objective should be minimized. Instead of a single optimum, there exists a Pareto-optimal set of solutions among which one objective may only be improved at the cost of the other.

(d) Multiobjective optimization

Tradeoffs between the two objectives for both cases are plotted in Fig. 7. Despite the similar trends in the two objectives in Case 296B as shown in Fig. 6b. Figure 7b shows that there also exists a Pareto-optimal set, although much smaller than in Case 290C. Note that in Case 290C, significant reductions in P_{diff} can be realized while incurring a small penalty in T_{diff}. Combined with the fact that pressure fluctuations play a more important role in determining the cavitation dynamics and the loadings on fluid machinery, this nonlinear tradeoff strongly favors reducing P_{diff}, suggesting an optimal value of about $C_{dest} = 0.65$, which also coincides with one of the Pareto-optimal solutions in Case 296B. This is also the value

used for other liquid nitrogen cases in Ref. [30], suggesting that the optimum is insensitive to differing thermal effects, since these cases correspond to different operating temperatures.

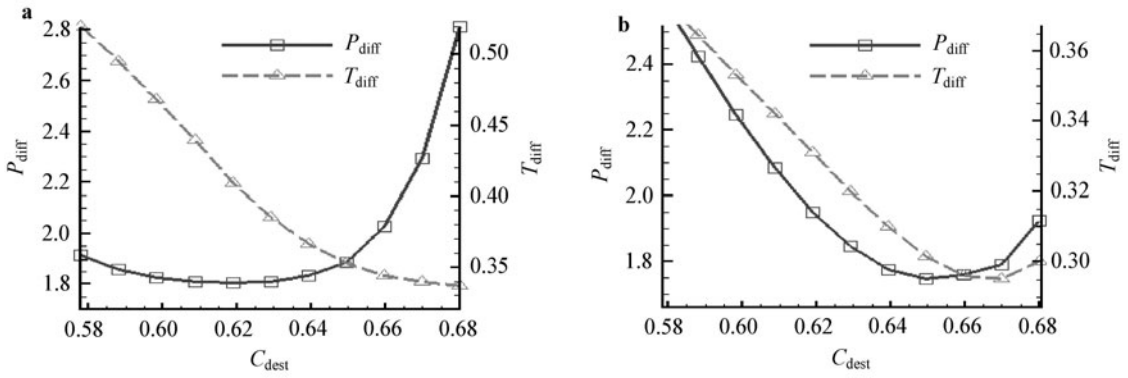

Fig. 6 Location of points (C_{dest}) and corresponding (P_{diff} is shown on the left y-axis, and T_{diff} is shown on the right y-axis) used for calibration of the cryogenic cavitation model

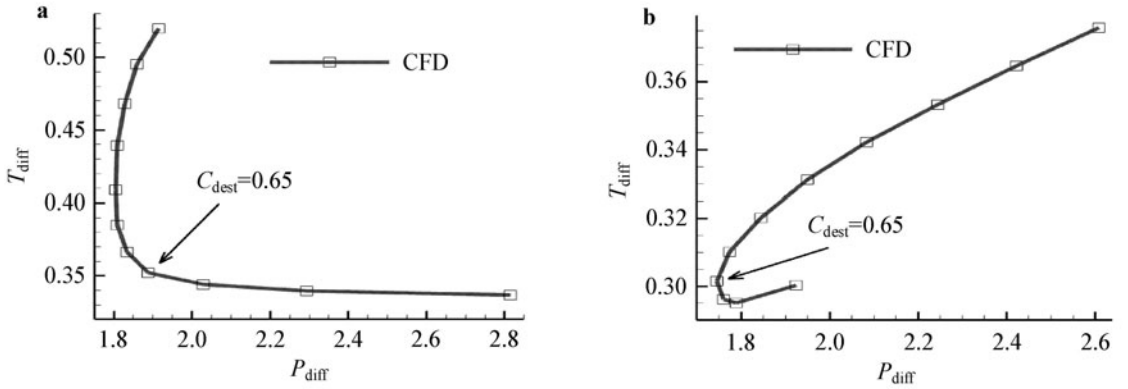

Fig. 7 Pareto fronts showing tradeoffs between objectives for both cases. **a** 290C; **b** 296B

This exercise has helped to validate the model parameter values. Note that since the model parameters are material dependent, the optimal evaporative parameter will vary with different cryogenic fluids. For example, repeating the process with liquid hydrogen showed that the optimal value should be $C_{dest} = 0.78$.

3.1.3 Major outcome

To assess the effects of model parameters and material property uncertainties on the predictive performance of the cryogenic cavitation model, we select C_{dest}, C_{prod}, ρ_v, and L as design variables and computed predictive errors in the pressure (P_{diff}) and temperature (T_{diff}) distribution. The KRG model is found to be the most suitable surrogate model due to its PRESS value and independent test point prediction. Global sensitivity analysis shows that the performance of the current cavitation model is affected most by the evaporative and vapor density terms, while the condensation term is not important at all within this design space, and the latent heat is significant only in temperature prediction. This enabled a reduction in the problem dimensionality, allowing the evaporative term to be optimized to minimize prediction error of the cavitation model when compared to experimental data. Although a Pareto front is found demonstrating tradeoffs between the pressure and temperature prediction, we recommend a value of $C_{dest} = 0.65$ due to the large gains available in pressure prediction at a small sacrifice in temperature prediction. Furthermore, this optimum is not affected by the different thermal effects from our current selected cases.

3.2 Dielectric barrier discharge for flow and thermal management

The DBD plasma actuator is a flow control device that is comprised of two asymmetrically placed electrodes separated by a dielectric barrier (insulator) and driven by the kilohertz radio frequency AC or pulses with kilo-volt amplitude as shown in Fig. 8. The discharge generates a weakly ionized gas and charged particles influenced by the electric

field can deliver momentum to the neutral particles [31,32]. Asymmetric geometry and charged particle dynamics, as a result, contribute to generate a unidirectional wall jet type flow [33,34].

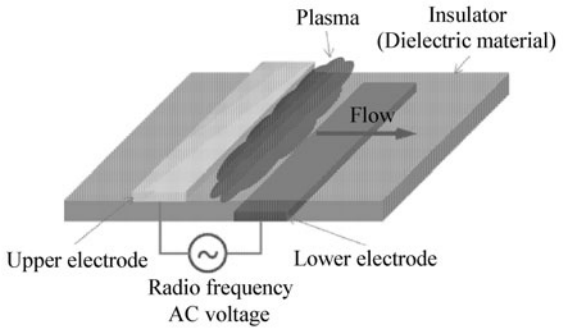

Fig. 8 Dielectric barrier discharge actuator configuration

In spite of the inherent advantages (no moving parts and vast control potential) of the DBD actuator, little insight is available regarding efficient operating conditions to accommodate various performance needs. With relatively high magnitudes of applied voltage (15 kV at 5–10 kHz AC) required for a uniform discharge, the force per unit width generated by a single actuator is less than 10 mN/m in air [35]. The flow velocity induced by a single actuator is usually less than 5 m/s for pulsed input voltage [36] as well as sinusoidal voltage waveforms [37]. In their efforts to understand the operating mechanism and possible optimal conditions for the actuator, various researchers have conducted parametric studies in terms of the waveform and frequency of the applied voltage, actuator geometry, and dielectric constant [37–39].

Furthermore, the efforts in numerical analysis to enhance or optimize the actuator's performance are hindered by the disparity in time and length scale inherent in the discharge dynamics and its influence on neutral flow. The first-principle-based DBD simulation is very expensive due to the multi-physics phenomena (such as ionization/recombination, charged particle drift, and discharge cycle) and often infeasible for design purposes. Furthermore, for an application to an airfoil of $O(10)$ cm chord, for example, there is $O(10^3)$ difference between the convective time scale of the induced airflow and the DBD operation frequency, which are $O(10^{-1})$ second and $O(10^4)$ Hz, respectively. As a result, it is critical in designing a flow and/or thermal management system using the DBD actuator to attain a reliable approximate model with computational efficiency.

The present study focuses on understanding the effect of three chosen parameters—waveform and frequency of the applied voltage and dielectric constant of the insulator—on the DBD actuator performance characterized by power input and generated force using surrogate models. The main objective is to assess the importance and impact of those variables, which have significant interplay on the actuator performance. The accuracy of each surrogate model for this application is also addressed, and the surrogate models with reasonable accuracy are shown to successfully refining the design space and resolving the region of interest with higher accuracy.

3.2.1 Physical model

The DBD actuator is modeled with the continuity and momentum, and electric field equations derived from the Boltzmann and Maxwell's equations, respectively. Since the atmospheric pressure is sufficiently high to assume local thermodynamic equilibrium, the fluid model is reasonably accurate and the local electric field density (E/N) can be used to approximate the phenomena related to the collision processes—ionization/recombination, diffusion and drift—instead of solving the energy equation [40]. Governing equations are given as Eq. (18) to Eq. (20) for only two species He^+ (subscript $p = i$) and electron (subscript $p = e$) for simplicity in this paper. S_{ie} and r are ionization and recombination rate coefficients, and μ and D are mobility and diffusivity of charged particles, respectively. q is electric charge of one species particle, and ε_0 is permittivity of vacuum.

$$\frac{\partial n_p}{\partial t} + \nabla \cdot (n_p \boldsymbol{u}_p) = n_e S_{ie} - r n_i n_e, \tag{18}$$

$$n_p \mu_p \boldsymbol{E} - \nabla(n_p D_p) = n_p \boldsymbol{u}_p, \tag{19}$$

$$\nabla \cdot (\varepsilon_d \boldsymbol{E}) = \frac{q_i n_i - q_e n_e}{\varepsilon_0}. \tag{20}$$

Equation (19) is the well-known drift-diffusion equation, which is valid also for ions in high pressure (atmospheric regime) discharge. To solve this set of equations, the source terms are handled with 4th-order backward differentiation formula (BDF) and the Poisson equation with the algebraic multigrid method, and the second-order central difference and upwind methods are employed for the diffusion and convection terms, respectively [41]. The charged particle densities and electric field are coupled by solving the Poisson equation between the predictor and corrector steps where the first order source splitting is used as noted in Ref. [40]. The coefficients of gaseous properties of helium regarding particle collisions and ionization/production are obtained from Refs. [31,32,42].

The computational domain with the actuator geometry is presented in Fig 9. The thickness of the insulator (h_d) is set as 0.5 cm and the lengths of upper (l_eu) and lower electrodes (l_el) are 0.2 cm same as the gap distance (d_e). The applied voltage to the upper electrode has sinusoidal shape with 1 kV amplitude but the positive-to-negative half cycle ratio r_f can be varied. Boundary conditions for the charge species at the dielectric surface are set to satisfy the current continuity that allows the accumulation of particles, and only electrons are allowed to be absorbed in the upper electrode without the secondary emission. Gas pressure of helium is

set as 300 mmHg, and the ion temperature is 300 K. The electron temperature is calculated as a function of the local electric field strength using a local field approximation approach, which is discussed in detail in Ref. [41].

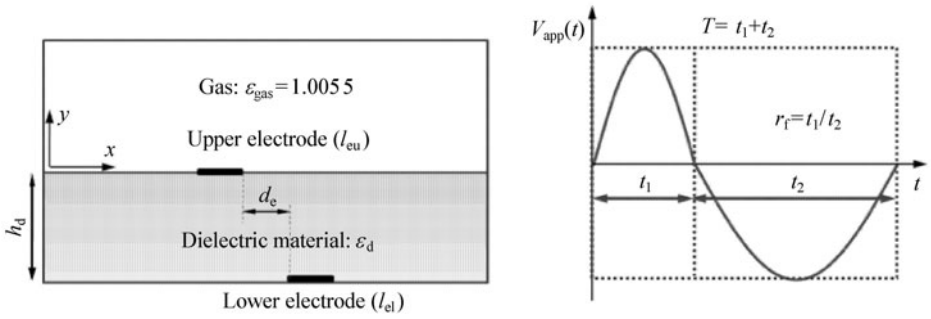

Fig. 9 Computational domain and applied waveform

3.2.2 Surrogate modeling process

3.2.2.1 Design of experiments and cross-validation

Among the many possible parameters affecting the actuator performance, three are chosen as design variables to assess their impact on the actuator efficiency.

The dielectric constant of the insulator material (ε_d), frequency of the applied voltage (f_v) and positive-to-negative half cycle ratio (r_f) are chosen for this study because they are among the key parameters which have non-simple effects on the resultant force by affecting both the peak value of domain averaged force and asymmetry in its waveform [43]. The constraint of each design variable is devised by considering the existing choice of materials and the general working conditions of previous DBD actuators. The objective functions are chosen to represent the actuator performance, namely the time and domain averaged x-directional force ($F_{x,ST}$) and average power input to the circuit (P_T) based on the charge current through the upper electrode. The time and domain averaged Lorentzian force to the charged particles is assumed to be equivalent to the body force acting on the neutral gas, especially at atmospheric pressure conditions. The definitions and parameter ranges are presented in Table 4.

The first level design of experiments, level 0 using the combination of 15 FCCD points and 5 LHS points and the simulation result of ε_d for those 20 points are presented in Fig. 10. Although the sampled points are well distributed in the design space, the response points cluster in some parts of the response space as in Fig. 10.

The surrogate models are obtained using these sampled points and their PRESS errors are presented in Table 5. Due to the insufficient number of sampled points and their complex responses, significant PRESS errors exist at this level especially in force prediction. For this case the KRG model shows the best performance in predicting the force while the PWS model does the same for power.

Table 4 Design variables, constraints, and objective functions

Design variable	Constraint
Dielectric constant of insulator ε_d	$2 \le \varepsilon_d \le 15$
Frequency of the applied voltage f_v/kHz	$5 \le f_v \le 20$
Positive-to-negative polarity time ratio r_f	$0.5 \le r_f \le 1.5$
Objective function	**Definition**
Time and domain averaged x-directional force $-\lvert F_{x,ST}\rvert/(\mathrm{mN\cdot m^{-1}})$	$F_{x,ST} \equiv \frac{1}{ST}\int_S\int_T F_x(\bar{r},t)\mathrm{d}t\mathrm{d}\bar{r}$
Power input for one cycle by the charge current through the upper electrode P_T/W	$P_T \equiv \frac{1}{T}\int_T I(t)V_{app}(t)\mathrm{d}t$ where $I(t) \equiv \int_{l_{eu}} (q_i n_i(t)u_{y,i}(t) - q_e n_e(t)u_{y,e}(t))\mathrm{d}x$

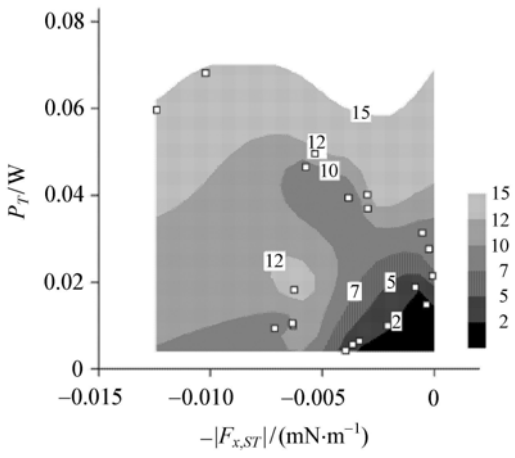

Fig. 10 Contours of ε_d with simulation results in objective function space in level 0

In order to explore the objective function distribution corresponding to the design space, a grid with 31^3 points evenly distributed in the whole design space is employed, and the result using the PWS is presented in Fig. 11. It can be observed that the Pareto front is not continuous and there are two distinct regions that are marked with two windows and correspond to the higher magnitude of force generation. Though the two regions lie on the same side of the force axis due to our adopting the absolute values of the force, the one with higher power corresponds to the negative (minus x-direction in Fig. 9) force generation, and the lower to the positive. On the other hand, the region corresponding to the positive force generation ensures a gain in force generation with much lower power.

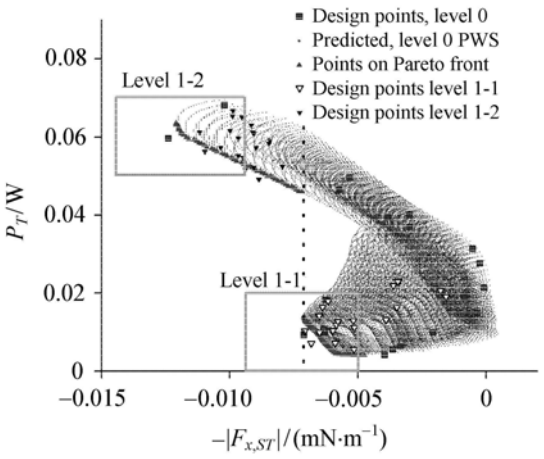

Fig. 11 Design and predicted points and Pareto fronts by the PRESS weighted surrogates in level 0

In Fig. 11, since the distribution of sampled points near the Pareto front are too sparse to resolve the regions of interest properly, two windowed regions are used as the constraints for design space refinement.

Level 1-1, low power region

$$-0.009 \le -|F_{x,ST}| \le -0.005\,(\mathrm{mN/m}), \quad 0 \le P_T \le 0.02\,(\mathrm{W})$$

Level 1-2, high power region

$$-0.014 \le -|F_{x,ST}| \le -0.009\,(\mathrm{mN/m}),$$
$$0.05 \le P_T \le 0.07\,(\mathrm{W})$$

The design variable constraints corresponding to these objective function constraints, namely design-space-constraints are generated based on the surrogate models at level 0. In order to generate the constraint surfaces, responses of a set of grid points uniformly distributed in the design space are obtained by using the surrogate models, and the surfaces confining the points whose responses satisfy the objective function constraints are then specified. Although the PWS has a smaller PRESS error in P_T as presented in Table 5, the design space confined by its design-space-constraints is included in that of the KRG model, and the refined regions are chosen conservatively to cover as much space as possible.

Table 5 PRESS errors of the surrogate models in level 0

	$-\lvert F_{x,ST}\rvert$	P_T
KRG	0.002 0 (16)*	0.003 2 (5.0)
PRS	0.0027 (22)	0.003 3 (5.2)
RBNN	0.0095 (77)	0.006 3 (9.9)
PWS	0.0028 (23)	0.002 3 (3.6)

*: ( ) % = 100 ×PRESS/($X_{\max}$−$X_{\min}$), $X = -|F_{x,ST}|$ or P_T in level 0.

Figure 12 shows the iso-force, iso-power surfaces and the design-space-constraint surfaces based on the KRG model (blue is for the lower bounds and red the upper bounds). Considering the lower and upper bounds of the objectives, each level has one refined space along with constraint surfaces. Since these surfaces are contours of constant force or power, based on their slopes it can be said that the force generation is relatively less sensitive to the dielectric constant than power.

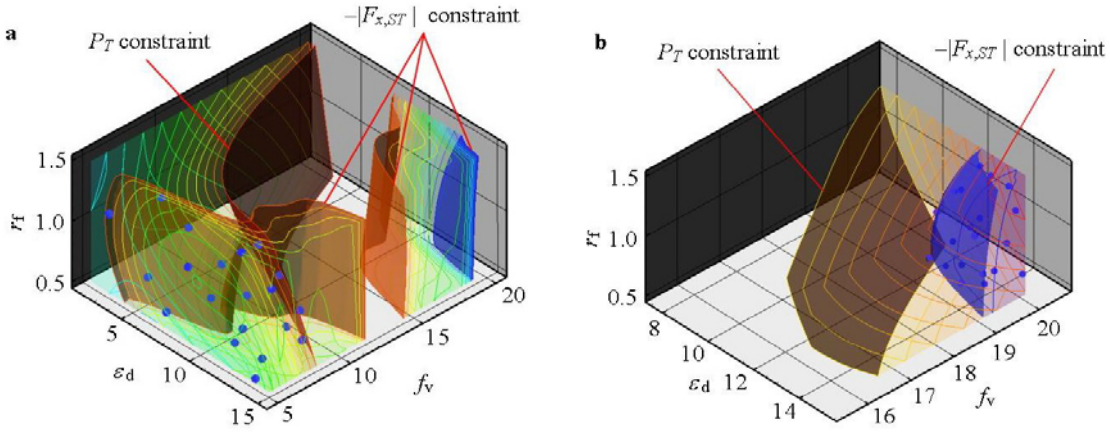

Fig. 12 Constraints, contours and design points for design space refinement. **a** Level 1-1: low power region; **b** Level 1-2: high power region

Since the design space corresponding to level 1-1 and level 1-2 constraint windows is irregular in shape, it is impossible to use the design of experiments for a rectangular hexahedron or sphere. For the design of experiments at the refined level, in order to sufficiently characterize the design space, the LHS is utilized to generate 5 000 points. Then, 20 points are selected by maximizing the minimum distance between those points. The design points generated by this approach are also shown in Fig. 12 along with the constraint surfaces.

3.2.2.2 Multiobjective optimization

To investigate the phenomena in the high- and low-power regions in depth, two points corresponding to the minimum $-|F_{x,ST}|$ condition are selected and the time history of the solution is compared in Figs. 13 and 14.

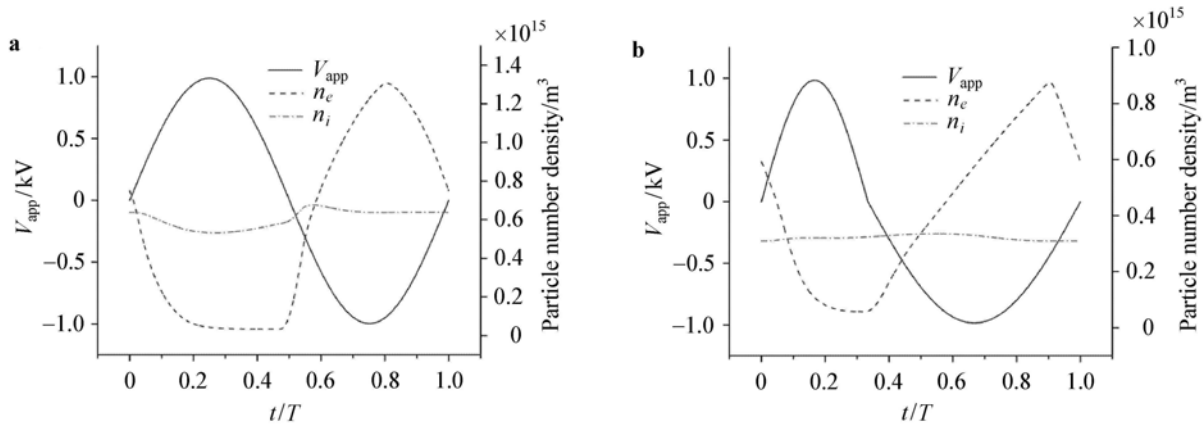

Fig. 13 Domain-averaged particle number density histories for two design points near the Pareto front. **a** Low power region: ε_d = 8.5, f_v = 5.0, r_f = 1.0; (b) High power region: ε_d = 15.0, f_v = 20.0, r_f = 0.5

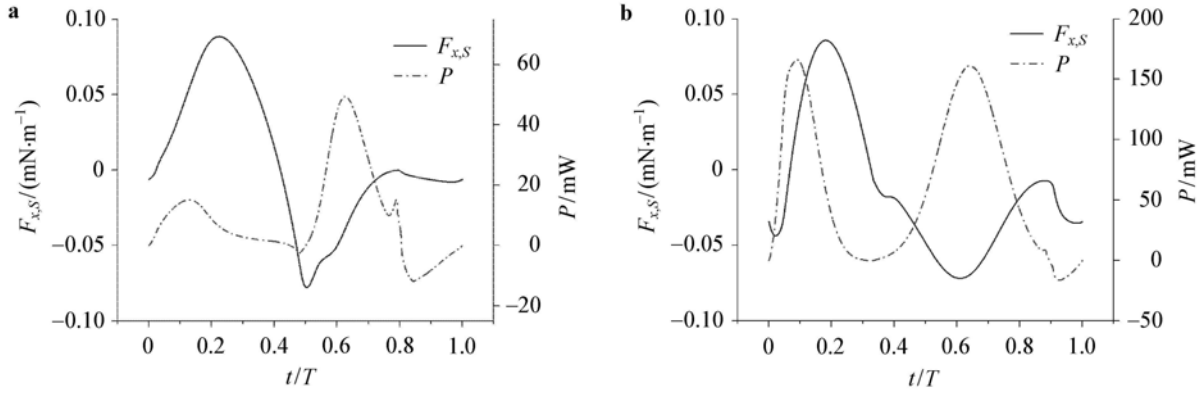

Fig. 14 Force and power histories for two design points near the Pareto front. **a** Low power region: ε_d=8.5, f_v = 5.0, r_f = 1.0; **b** High power region: ε_d = 15.0, f_v = 20.0, r_f = 0.5

In Fig. 13, it can be observed that for the case with lower frequency that belongs to the low power region, domain-averaged ion number density is higher. This can be explained by considering the fact that lower frequency allows more time to generate the particles, which is consistent with that found in Ref. [43]. The electron saturation instances in these cases—about t/T = 0.8 in the low power and 0.9 in the high power—coincide with the start of plateau or second dip in Fig. 14, which is also mentioned as one of the key factors affecting the solution with frequency.

From the force history results, one can deduce the effect of the positive-to-negative polarity time ratio, r_f. Although positive force belongs to the first half cycle and negative to the second, elongating the period of each part in the applied voltage source does not necessarily induce increased force either in positive or negative. While decreasing r_f, i.e. increasing the second half cycle corresponds to the decreased $-|F_{x,ST}|$ point in the high power region, increasing r_f does not mean increasing the duration of positive force cycle. The value of r_f corresponding to the maximum force generation in the positive x-direction is about 0.8 in the low power region according to the PWS model. The reason is that gener-

ating the positive force is mainly related to the plateau region of the second half cycle in $F_{x,S}$ time history as in Fig. 14.

3.2.2.3 Global sensitivity analysis

Figure 15 shows the result of the variance-based, non-parametric global sensitivity analysis for each refined level. Compared to the level 1-2, level 1-1 shows a stronger parameter correlation, which can be identified from the difference between total and main sensitivities. Also, the frequency of applied voltage, f_v in level 1-1 has a significant effect on both the average force and power. On the other hand, in the high power region (level 1-2) the effect of the positive-to-negative time ratio, r_f is prominent compared to that of f_v while the insulator dielectric constant is always important.

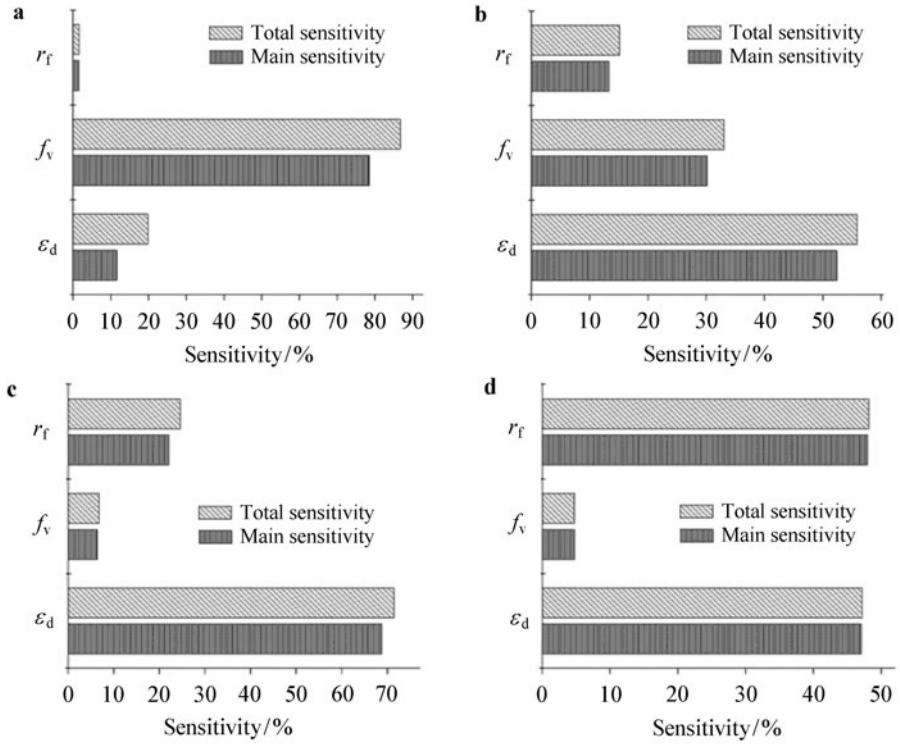

Fig. 15 Global sensitivity indices for the average force and power. **a** $F_{x,ST}$, level 1-1; **b** P_T, level 1-1; **c** $F_{x,ST}$, level 1-2; **d** P_T, level 1-2

3.2.3 Major outcome

Multiple branches of Pareto front within two regions apart from each other in the original design space are observed. In these low and high power regions, the orientation of the time-averaged force, degree of correlation between design variables and their global sensitivity indices are very different. The results can be used to enhance the performance of the actuator by devising effective control variables and understanding their influence on performance. The major impacts of design variables on the objectives are summarized below.

The dielectric constant of the insulator affects the amount of charged particle clouds above the insulator wall during the second half cycle. With a smaller constant, particle clouds thicken, increasing the asymmetry between the two half cycles. As a result the average force, F_x increases. On the other hand it also affects the density of the charged particle layer on the insulator surface. With a larger constant, a higher electric field is produced, resulting in the increase of F_x magnitude, but along the negative direction.

The applied voltage frequency affects the amount of overall charged particle generation. With a higher frequency, the discharge duration and the asymmetry between the two half cycles decrease, resulting in a larger F_x along the negative direction. Higher frequency accompanied by high dielectric constant induces larger power usage.

The positive-to-negative polarity time ratio also contributes to the overall charged particle generation. With a larger ratio, the first half cycle discharge becomes more prominent. As a result, F_x increases. On the other hand, the amount of charged particle clouds above the insulator wall during the second half cycle is also influenced. The larger ratio induces a smaller level of charged particle generation, which means insufficient electric field for the plateau region in the second half cycle. As a result F_x decreases.

Having demonstrated the use of global sensitivity analysis and Pareto front for mapping the design space in the preceding case studies, we conclude with a study on the model-

ing of lithium ion battery cells, where a reduction in problem dimensionality is shown to provide significant performance gains for the surrogate model.

3.3 Li-ion battery modeling

Li-ion batteries offer distinct advantages over other battery technologies due to their high energy density and low weight. However, despite significant experimentation and modeling effort, the competing effects of operational, geometric, and material parameters on battery performance are still not well understood. This may be attributed in part to the disparity in the measurement of material properties, such as the diffusion coefficient and electronic conductivity of the active materials, as well as the large number of variables and the difficulty of tuning them for experimental studies. Although various parametric studies have examined the role of individual design variables on cell performance capabilities, the combined effects of simultaneously varying several design variables and the relative magnitudes of their influence have not been established. Cross-interactions between variables are especially important as they may be responsible for critical design regions that can not be identified by adjusting individual variables. These critical design regions are particularly useful in battery design due to the aforementioned limited ability to tune certain material properties, as well as the varying discharge rates experienced in the cell during operation.

Due to these considerations, as well as the fact that there are often multiple competing objectives such as gravimetric and volumetric energy density, power, and cycle life, a comprehensive examination and comparison of the role of various design variables on cell performance requires a systematic and efficient mathematical framework. In this study, we seek to use surrogate-based analysis tools to construct models that can efficiently and accurately predict the specific energy and power of a Li-ion cell with respect to the cycling (or discharge) rate and the size and ion diffusivity and electronic conductivity of the active solid material. These models can thus be used to conduct global sensitivity analysis to identify critical design thresholds, observe combined effects due to cross-interactions, and quantify the relative importance of various parameters under different scenarios. An improved understanding of the most important performance-limiting factors will ultimately aid in cell optimization.

3.3.1 Physical model

In this study, the discharge process of a cell consisting of an MCMB 2 528 graphite anode and a lithium manganese oxide (spinel) cathode is modeled using a porous electrode formulation. In this model, the continuum-scale governing equations are solved in a pseudo-2D domain spanning the thickness of the cell and including assumed spherical particles at nodes in the positive and negative electrodes. The spherical particles are used to account for the effects of particle size, by solving the diffusion equation for the ion concentration within the particle

$$\frac{\partial c_1}{\partial t} = D_{\mathrm{s}}\left(\frac{\partial^2 c_1}{\partial r^2} + \frac{2}{r}\frac{\partial c_1}{\partial r}\right), \tag{21a}$$

with boundary conditions

$$\frac{\partial c_1}{\partial t} = 0, \qquad \text{at} \quad r = 0, \tag{21b}$$

$$\frac{i_{n,j}}{F} = -D_s\frac{\partial c_1}{\partial r}, \qquad \text{at} \quad r = R_{s,j}, \tag{21c}$$

where $j = n$ (anode) or p (cathode). In the liquid electrolyte

$$\varepsilon\frac{\partial c_2}{\partial t} = \nabla\cdot(D_2^{\mathrm{eff}}\nabla c_2) + \frac{1-t_+^0}{F}\nabla\cdot\boldsymbol{i}_2 - \frac{\boldsymbol{i}_2\cdot\nabla t_+^0}{F}. \tag{22}$$

In Eqs. (21) and (22), c_1 and c_2 denote the Li-ion concentrations in the solid and liquid phases, respectively. A gradient of the chemical potential is the driving force for the Li-ion diffusion across the width of the cell. In the existing model, the chemical kinetics at the particle-electrolyte interface is described using the Butler–Volmer equation, in which the flux at the particle surface is a function of the exchange current density and the surface overpotential, as shown in Eq. (23)

$$i_{n,j} = i_{0,j}\left[\exp\left(\frac{\alpha_{\alpha,j}F}{RT}\eta_j\right) - \exp\left(-\frac{\alpha_{\alpha,j}F}{RT}\eta_j\right)\right], \tag{23}$$

where $\eta_j = \varphi_1 - \varphi_2 - U_{\mathrm{OCP}}$ is the surface overpotential. The surface overpotential is estimated based on the electrical potentials in the solid (φ_1) and liquid (φ_2) phases, using Eqs. (24) and (25)

$$\nabla\cdot(\sigma\nabla\varphi_1) - J = 0, \tag{24}$$

$$\nabla\cdot(\kappa\nabla\varphi_2) + \nabla\cdot[\kappa_D\nabla(\ln c_2)] + J = 0. \tag{25}$$

The volumetric reaction current J is calculated using Eq. (26), where $\varepsilon_{1,p}$ ($\varepsilon_{1,n}$) and $R_{s,p}$ ($R_{s,n}$) are the porosity and particle size in the positive (negative) electrode, respectively. Further details of the porous electrode model can be found in Refs. [44–46].

$$J = \begin{cases} \left(\dfrac{3\varepsilon_1}{R_s}\right)_p i_{n,p}, & \text{in the positive electrode,} \\ 0, & \text{in the separator,} \\ \left(\dfrac{3\varepsilon_1}{R_s}\right)_n i_{n,n}, & \text{in the negative electrode.} \end{cases} \tag{26}$$

3.3.2 Surrogate modeling process

3.3.2.1 Design of experiments and cross-validation

The design variables considered in this study and their corresponding ranges are summarized in Table 6. Since the focus of the study is on the cathode, the particle size and material properties apply to that electrode only. The selected cycling rate range corresponds to typical automotive application requirements, while the particle sizes are consistent

with those found in real electrodes [47]. The diffusion coefficient is known to be sensitive to the cell's state of charge, and reported values in the literature vary widely due to differences in electrode microstructure and measurement techniques [48]. Therefore, a wide diffusivity range needed to be considered to remain consistent with values reported in the literature. Further details of appropriate choices for the design ranges can be found in Ref. [49]. A fixed thickness is assigned to all cell components: 100 μm for each electrode and 25 μm for the separator and each current collector. A uniform initial state of charge in each electrode is specified for each simulation, and the cell is discharged until the termination voltage of 2.0 V is reached.

Table 6 Design variables and corresponding ranges

Variable	Range
Cycling rate C/C	0.1–4
Particle radius $R_{s,p}/\mu$m	0.2–20
Diffusivity $D_s/(\mathrm{m}^2\cdot\mathrm{s}^{-1})$	$0.1–10\times10^{-13}$
Conductivity $\sigma/(\mathrm{S}\cdot\mathrm{m}^{-1})$	1–100

Three types of surrogate models are considered in this study: polynomial response surface (PRS), kriging (KRG), and radial basis neural network (RBNN). For the kriging models, first and second-order polynomial regressions are tested. In the RBNN models, the spread coefficient and error goal parameters are tuned to adjust the fit; however, the total number of neurons is fixed. For cross-validation of the PRS models, the adjusted coefficient of determination R^2_{adj} is considered in addition to PRESS and independent test point prediction.

A preliminary design of experiments consisting of 25 points in a FCCD arrangement is initially selected to roughly evaluate the magnitude of effects of all design variables before constructing a comprehensive design of experiments. Since achieving a good surrogate model fit in a high-dimensional design space can be difficult [11], this first step is done to check for any variables that could be immediately removed from consideration, thus reducing the problem dimensionality. It is found that in all cases within the face-centered design, the effect of the electronic conductivity is negligible even when varied between its minimum and maximum values. This can also be verified with test points in the interior of the design space to check for interactions with other variables; in all cases varying the conductivity within the selected range causes less than a 1% change in the total cell energy. As a result, all subsequent analysis is performed on a reduced design space consisting of only the first three variables listed in Table 6.

The initial design of experiments consisted of the 15 non-redundant points from the previous four design variable FCCD, in addition to 35 LHS points. However, error measures computed based on this initial design shows that it is too sparse to achieve sufficient model fit, with the minimum PRESS value being over 20% of the mean function value. Additionally, the region with high cycling rate, large particle size, and low diffusivity shows a sharp gradient in the specific energy, and the sparse distribution of points in this region contributes to poor overall model fit. To ensure a greater density of points in this sharp gradient region, a domain refinement is performed with an additional 100 design points in a logarithmic distribution.

Although this refinement improves model prediction in the previously sparse region, it also causes a shift in fidelity, leaving unacceptably large prediction errors elsewhere in the design space. To improve model fit in the entire design space, another refinement consisting of 165 design points selected using Latin hypercube sampling is made, resulting in a total of 315 points in the design of experiments. A kriging model constructed using this data set yields a PRESS value of 3.0% of the mean function value and a mean prediction error of 2.5% at 64 test points, suggesting a sufficient model fit to perform global sensitivity analysis.

3.3.2.2 Global sensitivity analysis

Sensitivity indices computed from a wide range of surrogate models all indicate that the effects due to all three variables are strong, preventing further problem dimensionality reduction by direct variable elimination. However, it is also found that the global sensitivity indices vary among the different regions of the design space. As shown in Fig. 16, the effect of diffusivity vanishes in the diffusivity range above some critical value at about 1×10^{-13} m^2/s. This diffusion-independence in the high-diffusivity range presents an opportunity to split the design space into multiple regions in which the problem dimensionality may be reduced for separate, more refined analysis.

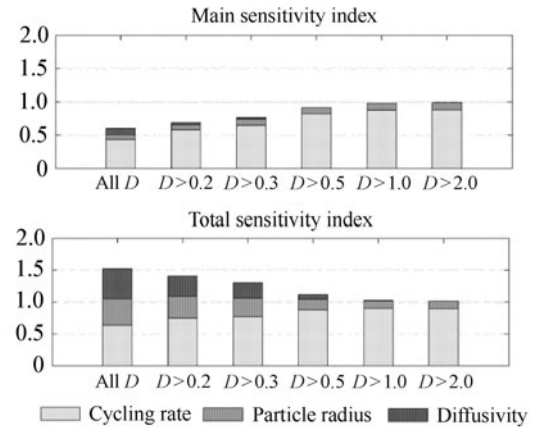

Fig. 16 Sensitivity indices for KRG models constructed on selectivity diffusivity ranges (10^{-13} m^2/s)

3.3.2.3 Dimensionality reduction and design space splitting

Within the low-diffusion range, it is found that the specific

energy rapidly decreases with increasing discharge rate and particle size, as well as decreasing diffusivity. To further refine the analysis, we introduce a dimensionless time term τ to characterize the discharge and diffusion time scales

$$\tau = \frac{D_s}{R_{s,p}^2 C}. \tag{27}$$

As shown in Eq. (27), this dimensionless time parameter combines all three design variables into a single expression relating the relative rates of the discharge and diffusion processes in the cell. As shown in Fig. 17, the specific energy decreases for low values of this parameter, where the diffusion rate is low compared to the required discharge rate. Also note the clear monotonic trend for values of $\tau < 0.2$.

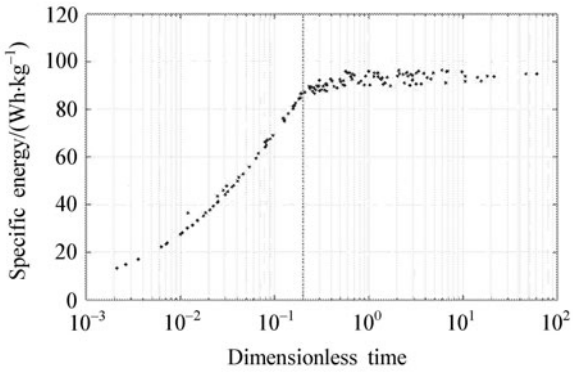

Fig. 17 Specific energy vs. dimensionless time, for $D_s < 1 \times 10^{-13}$ m^2/s

This suggests a further splitting of the diffusion-dependent region into a diffusion-limited region defined exclusively by the single dimensionless time parameter, and an intermediate region between the diffusion-limited and diffusion-independent regions, where all three variables are important. The process for splitting the design space and resulting sub-regions are summarized in Fig. 18.

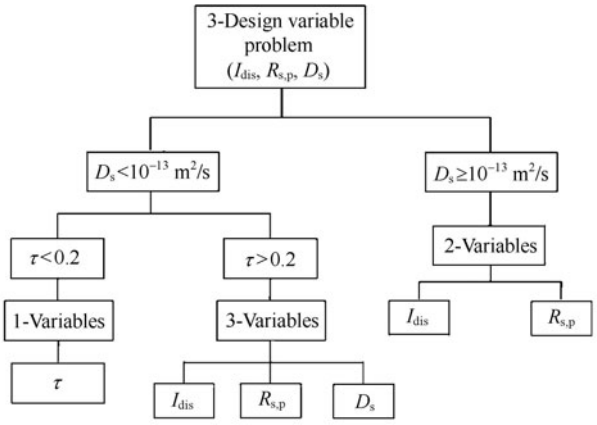

Fig. 18 Process for splitting design space into separate reduced-dimensionality regions based on sensitivity indices and critical diffusion values

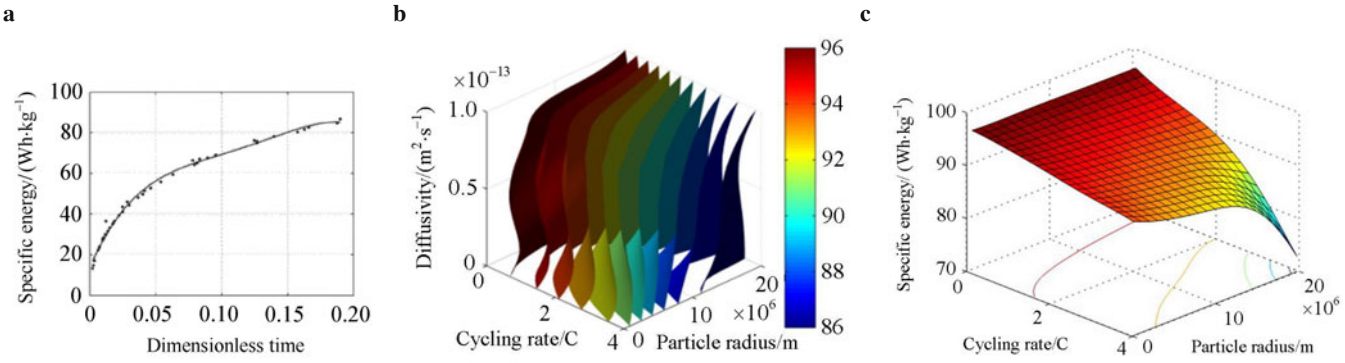

Fig. 19 Specific energy as a function of the design variables. **a** Diffusion-limited (1 DV); **b** Intermediate (3 DV); **c** Diffusion-Independent (2 DV)

To assess the effect of design space splitting on surrogate model fit, various error measures are computed for the best of each surrogate model type and compared between the non-split model for the entire design space and the split sub-regions. The results are summarized in Table 7, which shows significantly improved model fit in each split sub-region when compared to the single model for the entire domain. Perhaps more importantly, this improved model fit can be achieved without requiring any new data. Line and surface plots for the specific energy in the split sub-regions are shown in Fig. 19; the energy decreases rapidly at very low values of the dimensionless time parameter, as well as high cycling rates and large particle sizes. A weaker diffusivity effect can be observed in Fig. 19b; however, the diffusivity effects are strongest in the diffusion-limited region where they are reflected in the dimensionless time parameter.

Table 7 Effect of design space splitting on performance metrics

Surrogate	Parameter	Non-split	Split		
			Diffusion-limited	Intermediate	Diffusion-independent
	Design points	315	42	32	236
	Design variables	3	1	3	2
PRS	R^2_{adj}	0.875	0.995	0.997	0.932
	RMSE/%	6.98	3.99	0.09	0.87
	PRESS/%	8.11	6.29	0.84	0.95
	RMS test error/%	10.0	—	0.48	—
	Max test error/%	34.6	—	1.46	—
KRG	PRESS/%	3.50	5.21	0.43	1.53
	RMS test error/%	5.24	—	0.65	—
	Max test error/%	21.2	—	1.96	—
RBNN	PRESS/%	6.05	—	1.39	4.63
	RMS test error/%	7.34	—	1.06	—
	Max test error/%	29.2	—	2.79	—

3.3.2.4 Multiobjective optimization

The preceding results have shown that specific energy can be increased by reducing the discharge rate. However, the discharge rate is also directly related to the battery cell's power output, another critical objective. Since the power is directly dependent on the discharge current, a competing effect can be expected between specific energy, which favors low cycling rates, and specific power, which favors higher rates. To quantify these competing effects, a Pareto front is constructed from additional randomly sampled points and fitted with the split surrogate models shown in Table 7.

Specific power data are fit by constructing an additional 4th order PRS model. The resulting Pareto front is shown in Fig. 20.

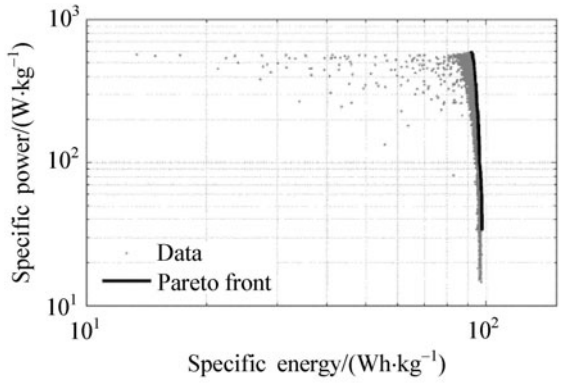

Fig. 20 Pareto front showing tradeoff between specific energy and specific power

The front shows stiffness in favor of high power, which can be achieved with relatively little sacrifice in energy. However, a greater amount of scatter in the specific energy data can also be observed as the specific power is increased. This suggests that the cell performance becomes increasingly sensitive to the other design variables as the cycling rate is increased, resulting in a greater penalty for large particle size or low diffusivity in the cathode.

3.3.3 Major outcome

For simplicity, it is often preferable to represent a full design space with a single surrogate model. However, due to the difficulty encountered in attempting to achieve a reasonable model fit with a single global surrogate, a split design space strategy is adopted instead. Although the splitting of the design space does not provide any advantage in terms of computational speed, it does allow for much improved surrogate model fit as shown in Table 7, even in the intermediate region in which a reduction in dimensionality did not occur. This is likely due to differing dominant physical phenomena within the design space, as suggested by the shift in fidelity caused by the initial domain refinement and the dimensionless time scale analysis. The improved surrogate model performance is critically important to the construction of a meaningful Pareto front to study the competition between specific energy and specific power.

One limitation of the current approach is that the physical model does not account for the microstructure of the electrode material, which can have a significant impact on the overall cell performance. To address this limitation, Gupta et al. [50] have recently developed a framework based on the mechanics and transport approach presented by Zhang

et al. [51,52] to accomplish the first stage of a multiscale model by quantifying the impact of the electrode architecture on the microscale reaction density and transport properties and formulate reduced-order models for the same. In their study, surrogate models have been constructed on effective transport properties to provide an opportunity for combining physics at various scales in a computationally efficient manner. Different particle packing arrangements have been analyzed for the calculation of effective transport properties and reaction density that appear in the porous-electrode formulation due to the volume-averaging process. To bridge the gap between microscopic simulations of particle clusters and cell-level simulations and estimation of volume-averaging closure terms, Li-ion concentration, electric potential and their gradients in the solid and electrolyte phase have been chosen as design variables for formulating reduced-order models using surrogate-based analysis.

For the microscopic simulations in Ref. [50], each point of the DOE identifies the local values of the design variables at a given node on the macroscopic mesh of a Li-ion positive electrode. As in the cell-scale simulations, the surrogate models trained included polynomial response surface (PRS), kriging (KRG) and radial-basis neural network (RBNN). The design of experiments contained a sufficient number of data points to fit at most a 3rd order polynomial surface. For kriging, both first- and second-order polynomial regression models were considered with the Gaussian and cubic spline correlation functions. The best kriging model was obtained by optimizing the kriging model parameters to minimize the maximum prediction error at selected test points. For a second-order polynomial regression and Gaussian correlation model, the prediction errors at test points were greatly reduced. Additionally, PRESS values were also significantly reduced with the optimized kriging model.

Based on the second-order regression with Gaussian correlation kriging model, global sensitivity analysis has been conducted to understand the relative importance of concentrations, electric potentials and their gradients on the normalized reaction density. The main and total index for the three main design variables computed from the kriging model with least error measures is shown in Fig. 21. The indices computed for the other variables, namely electrolyte concentration and gradients of concentrations and potentials in both phases, were found to be negligible and thus are not shown. Their study offers a clear step towards integration of the effect of microstructure into a macroscale simulation via a multiscale model. Note that an important advantage of using a surrogate framework to accomplish the scale bridging is that the framework allows the individual scale models to be refined separately. For example, data from additional microscopic simulations conducted for a greater range of porosity levels can be readily incorporated into the macroscopic model via refined surrogates.

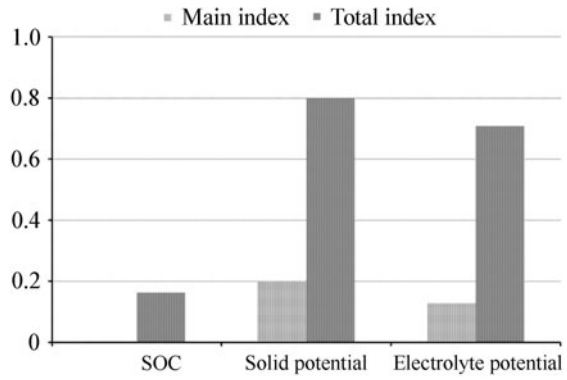

Fig. 21 Error measures obtained through different surrogate models trained on the design of experiments for prediction of normalized reaction density [50]

4 Conclusions

In this paper, we present three case studies that fall under different domains of engineering, namely cavitation, dielectric barrier discharge (DBD), and Li-ion batteries. The cost and time constraints associated with each of the problems are highlighted. To enable the design of better engineered systems, different criteria may be applied. Validated cavitation model parameters are needed that can predict its onset. On the other hand, operating and material conditions that achieve better performance goals are not known for DBD. In Li-ion batteries, the effect of simultaneous variation of several design variables on its performance should be quantified.

Surrogate modeling and analysis offers a unique design tool for each of these problems:

(1) The surrogate analysis is used to assess
   (a) the sensitivity of the cavitation model to parameters and uncertainties in the thermal-sensible material properties,
   (b) the impact of waveform, frequency and dielectric constant on DBD performance, and
   (c) the relative importance of discharge rate, particle size, diffusivity and conductivity of battery performance.

(2) The surrogate models can be particularly useful in analyzing competing objectives, such as the accuracy of temperature and pressure prediction in cavitation, power input and force generation in DBD, and specific energy and power in Li-ion batteries.

(3) The surrogate-based global sensitivity analysis facilitates identification of dominating and less-influential design variables. Based on the insight gained, dimensionality reduction can be conducted to reduce the complexity of the issues. This benefit is particularly significant for complex problems which are expensive to simulate/test

and involve a large number of design variables. For instance, it is shown that

(a) the condensation term has minimal influence on the cavitation model compared to the evaporation term,
(b) the dielectric constant is always influential, but the importance of frequency and time ratio alternates depending on low and high power capabililty, and
(c) the dimensionality of the battery case can be reduced based on the diffusivity of the solid, which could be ignored from the analysis beyond a certain critical value.

(4) In addition to sensitivity analysis, surrogate tools offer the capability to identify optimal solutions in regions where competing objectives may be present. In such cases, construction of a Pareto front can assist in elucidating the gain achieved by sacrificing the other objectives. In the context of the case studies presented, we show that multiple Pareto fronts, which may be disconnected with each other, may also exist, as evident in the case of DBD. For cavitation, it was shown that a selected value of the evaporation model parameter minimizes the pressure difference through a small penalty in the temperature difference. Since pressure prediction is more critical in design of components that may be subjected to heavy loads, the tradeoff between pressure and temperature is beneficial in this situation. In the case of Li-ion batteries, the high slope of the Pareto front suggests that substantial gain in power, which is desirable for power-tools and automotive applications, can be achieved through minor sacrifice in energy storage.

In summary, we have developed a surrogate-based framework to assess the role of design variables on multiple competing objectives for a wide range of engineering problems. The framework allows for both local and global domain refinement strategies to be utilized in conjunction with multiple error criteria to estimate and reduce uncertainties, since a single criterion may lead to high errors. These techniques prove to be very valuable in advancing the capabilities of surrogate modeling. The surrogate modeling frameworkalso offers a clear-step towards integration of the effect ofmulti-scale physics via scale-bridging and dimensionalityreduction. Similar approaches can be extended to numerousother mechanics, thermo-fluid and energy problems. Such an approach can further enhance the multi-scale approach previously developed in, e.g., Refs. [53–56].

References

1 Fletcher, R., Powell, M.J.D.: A rapidly convergent descent method for minimization. Comp. J. **6**, 163–168 (1963)
2 Papila, N., Shyy, W., Griffin, L., et al.: Shape optimization of supersonic turbines using global approximation methods. J. Prop. Power **18**, 509–518 (2002)
3 Shyy, W., Papila, N., Vaidyanathan, R., et al.: Global design optimization for aerodynamics and rocket propulsion components. Prog. Aero. Sci. **37**, 59–118 (2001)
4 McKay, M.D., Beckman, R.J., Conover, W.J.: A comparison of three methods of selecting values of input variables in the analysis of output from a computer code. Technometrics **21**, 239–245 (1979)
5 Myers, R.H., Montgomery, D.C.: Response Surface Methodology: Process and Product in Optimization Using Designed Experiments. (1st ed.) Wiley and Sons Inc. (1995)
6 Queipo, N.V., Haftka, R.T., Shyy, W., et al.: Surrogate-based analysis and optimization. Prog. Aero. Sci. **41**, 1–28 (2005)
7 Forrester, A.I.J., Keane, A.J.: Recent advances in surrogate-based optimization. Prog. Aero. Sci. **45**, 50–79 (2009)
8 Zones, D.R.: A taxonomy of global optimization methods based on response surfaces. J. Global Opt. **21**, 345–383 (2001)
9 Sacks J., Welch, W.J., Mitchell, T.J., et al.: Design and analysis of computer experiments. Statistical Science **4**(4), 409–435 (1989)
10 Lophaven, S.N., Nielsen, H.B., Sondergaard, J.: DACE—A Matlab kriging toolbox. Version 2.0, Technical Report, IMM-TR-2002-12, Technical University of Denmark, Denmark (2002)
11 Goel, T., Dorney, D.J., Haftka, R.T., et al.: Improving the hydrodynamic performance of diffuser vanes via shape optimization. Comp. Fluids **37**, 705–723 (2008)
12 Goel, T., Haftka, R.T., Shyy, W., et al.: Ensemble of surrogates. Struct. Multidisc. Optim. **33**, 199–216 (2007)
13 Goel, T., Haftka, R.T., Shyy, W.: Comparing error estimation measures for polynomial and kriging approximation of noise-free functions. Struct. Multidisc. Optim. **38**, 429–442 (2009)
14 Laslett, G.M.: Kriging and splines: an empirical comparison of their predictive performance in some applications. J. Amer. Stat. Assc. **89**(426), 391–400 (1994)
15 Meckesheimer, M., Booker, A.J., Barton, R.R., et al.: Computationally inexpensive metamodel assessment strategies. AIAA J. **40**(10), 2053–2060 (2002)
16 Sobol, I.: Sensitivity estimates for non-linear mathematical models. Math. Modeling Comput. Exp. **4**, 407–414 (1993)
17 Mack, Y., Goel, T., Shyy, W., et al.: Surrogate model-based optimization framework: a case study in aerospace design. Stud. Comp. Intel. **51**, 323–342 (2007)
18 Utturkar, Y., Wu, J., Wang, G., et al.: Recent progress in modeling of cryogenic cavitation for liquid rocket propulsion. Prog. Aero. Sci. **41**, 558–608 (2005)
19 Knapp, R.T., Daily, J.W., Hammitt, F.G.: Cavitation, McGraw-Hill, New York (1970)
20 Brennen, C.E.: Cavitation and Bubble Dynamics. Oxford Engineering & Sciences Series, Oxford University Press, New York (1995)
21 Venkateswaran, S., Lindau, J.W., Kunz, R.F., et al.: Preconditioning algorithms for the computation of multiphase mixture flows. J. Comp. Phys. **179**, 1–29 (2002)
22 Joseph, D.D.: Cavitation and the state of stress in a flowing liquid. J. Fluid Mech. **366**, 367–378 (1998)
23 Lemmon, E.W., McLinden, M.O., Huber, M.L.: REFPROP: Reference fluid thermodynamic and transport properties. NIST Standard Database 23, version 7.0 (2002)
24 Goel, T., Thakur, S., Haftka, R.T., et al.: Surrogate model-based strategy for cryogenic cavitation model validation and

sensitivity evaluation. Int. J. Numer. Meth. Fluids **58**, 969–1007 (2008)
25 Tseng, C.C., Wei, Y.J., Wang, G., et al.: Review: modeling of turbulent, isothermal and cryogenic cavitation under attached conditions. Acta Mechanica Sinica **26**, 325–353 (2010)
26 Tseng, C., Shyy, W.: Modeling for isothermal and cryogenic cavitation. Int. J. Heat Mass Trans. **53**, 513–525 (2010)
27 Wang, G., Senocak, I., Shyy, W., et al.: Dynamics of attached turbulent cavitating flows. Prog. Aero. Sci. **37**, 551–581 (2001)
28 Senocak, I., Shyy, W.: Interfacial dynamics-based modeling of turbulent cavitating flows, part-1: model development and steady-state computations. Int. J. Numer. Meth. Fluids **44**, 975–995 (2004)
29 Li, X., Wang, G., Yu, Z., et al.: Multiphase fluid dynamics and transport processes of low capillary number cavitating flows. Acta Mechanica Sinica **25**, 161–172 (2009)
30 Hord, J.: Cavitation in liquid cryogens II-hydrofoil. NASA CR-2156 (1973)
31 McDaniel, E.W.: Collision Phenomena in Ionized Gases. John Wiley & Sons, New York (1964)
32 Mitchner, M., Kruger Jr., C.H.: Partially Ionized Gases, John Wiley & Sons, New York (1973)
33 Roth, J.R., Sherman, D.M.: Boundary layer flow control with a one atmosphere uniform glow discharge surface plasma. 36th AIAA Aerospace Sciences Meeting and Exhibit, AIAA Paper 98-0328, Reno, NV (1998)
34 Shyy, W., Jayaraman, B., Andersson, A.: Modeling of glow discharge-induced fluid dynamics. J. Appl. Phys. **92**(11), 6434–6443 (2002)
35 Porter, C.O., Baughn, J.W., McLaughlin, T.E., et al.: Plasma actuator force measurements. AIAA J. **45**(7), 1562–1570 (2007)
36 Jukes, T.N., Choi, K., Johnson, G.A., et al.: Characterization of surface plasma-induced wall flows through velocity and temperature measurements. AIAA J. **44**(4), 764–771 (2006)
37 Forte, M., Jolibois, J., Moreau, E., et al.: Optimization of a dielectric barrier discharge actuator by stationary and non-stationary measurements of the induced flow velocity-application to airflow control. 3rd AIAA Flow Control Conference, AIAA Paper 2006-2863, San Francisco, CA (2006)
38 Abe, T., Takizawa, Y., Sato, S., et al.: A parametric experimental study for momentum transfer by plasma actuator. 45th Aerospace Sciences Meeting and Exhibit, AIAA Paper 2007-187, Reno, NV (2007)
39 Roth, J.R., Dai, X.: Optimization of the aerodynamic plasma actuator as an electrohydrodynamic (EHD) electrical device. 44th AIAA Aerospace Sciences Meeting and Exhibit, AIAA Paper 2006-1203, Reno, NV (2006)
40 Jayaraman, B., Tharkur, S., Shyy, W.: Modeling of fluid dynamics and heat transfer induced by dielectric barrier plasma actuator. J. Heat Trans. **129**, 517–525 (2007)
41 Jayaraman, B., Shyy, W.: Modeling of dielectric barrier discharge-induced fluid dynamics and heat transfer. Prog. Aero. Sci. **44**, 139–191 (2008)
42 Ward, A.L.: Calculations of cathode-fall characteristics. J. Appl. Phys. **33**(9), 2789–2974 (1962)
43 Jayaraman, B., Cho, Y., Shyy, W.: Modeling of dielectric barrier discharge plasma actuator. J. Appl. Phys. **103**, 053304 (2008)
44 Doyle, M., Fuller, T.F., Newman, J.: Modeling of galvanostatic charge and discharge of the lithium/polymer/insertion cell. J. Electrochem. Soc. **140**, 1526–1533 (1993)
45 Fuller, T.F., Doyle, M., Newman, J.: Simulation and optimization of the dual lithium ion insertion cell. J. Electrochem. Soc. **141**, 1–10 (1994)
46 Doyle, M., Newman, J., Gozdz, A.S., et al.: Comparison of modeling predictions with experimental data from plastic lithium ion cells. J. Electrochem. Soc. **143**, 1890–1903 (1996)
47 Lu, C.H., Lin, S.W.: Influence of the particle size on the electrochemical properties of lithium manganese oxide. J. Power Sources **97-98**, 458–460 (2001)
48 Zhang, D., Popov, B.N., White, R.E.: Modeling lithium intercalation of a single spinel particle under potentiodynamic control. J. Electrochem. Soc. **147**, 831–838 (2000)
49 Du, W., Gupta, A., Zhang, X., et al.: Effect of cycling rate, particle size and transport properties on Li-ion cathode performance. Int. J. Heat Mass Trans. **53**, 3552–3561 (2010)
50 Gupta, A., Seo, J.H., Zhang, X., et al.: Effective transport properties of $LiMn_2O_4$ electrode via particle-scale modeling. J. Electrochem. Soc. **158** A487–497 (2011)
51 Zhang, X., Sastry, A.M., Shyy, W.: Intercalation-induced stress and heat generation inside lithium-ion battery cathode particles. J. Electrochem. Soc. **155**, A542–552 (2008)
52 Zhang, X., Shyy, W., Sastry, A.M.: Numerical simulation of intercalation-induced stress in Li-ion battery electrode particles. J. Electrochem. Soc. **154**, A910–916 (2007)
53 Sozer, E., Shyy, W.: Modeling of fluid dynamics and heat transfer through porous media for liquid rocket propulsion. International Journal of Numerical Methods for Heat and Fluid Flow **18**, 883–899 (2008)
54 Martin, A., Saltiel, C., Shyy, W.: Heat transfer enhancement with porous inserts in recirculating flows. ASME Journal of Heat Transfer **120**, 458–467 (1998)
55 Shyy, W., Correa, S.M., Braaten, M.E.: Computation of flow in a gas turbine combustor. Combustion Science and Technology **58**, 97–117 (1988)
56 Shyy, W., Thakur, S.S., Ouyang, H., et al.: Computational Techniques for Complex Transport Phenomena. Cambridge University Press, New York, hardcover (1997), paperback (2005)